

Basic Properties of ZnO, GaN, and Related Materials

T. Hanada

Abstract. Structural, elastic, and electronic properties of the group-III nitride and the group-II oxide semiconductors are introduced here with basic material parameters. These materials generally have uniaxial anisotropy due to the wurtzite-type crystal structure. The basic formulae on the elastic properties and the electronic structures characterized by the uniaxial anisotropy are presented in this chapter.

1.1 Introduction

The group-III nitride and the group-II oxide semiconductors have direct bandgaps, which cover the ultraviolet to infrared energy range. Particularly, the wide bandgap of AlN, GaN, and ZnO is favorable for short-wavelength light emitting devices and high-power devices. Figure 1.1 shows the relation between bandgap energy and wurtzite lattice constant a or $1/\sqrt{2}$ of zincblende lattice constant a_{ZB} for AlN, GaN, InN, and their alloys [1].

Figure 1.2 shows bandgap energy and lattice constants of wurtzite $\text{Be}_x\text{Zn}_{1-x}\text{O}$ [2], $\text{Mg}_x\text{Zn}_{1-x}\text{O}$ [3, 4], and $\text{Zn}_{1-y}\text{Cd}_y\text{O}$ [4–6] alloy films. ZnO also attracts attention owing to the large exciton binding energy, which is expected to be favorable for high efficiency light emitting devices up to high temperatures. A set of basic data and related formulae on the structural, elastic, and electronic properties of the group-III nitride and the group-II oxide semiconductors will be introduced in this chapter.

1.2 Crystal Structure

1.2.1 Crystal Structure of Related Materials

Crystal structure of ZnO, AlN, GaN, and InN is usually the hexagonal wurtzite (WZ) type, which has nearly the same tetrahedral nearest-neighbor atomic coordination as cubic zincblende (ZB) type structure. As shown in

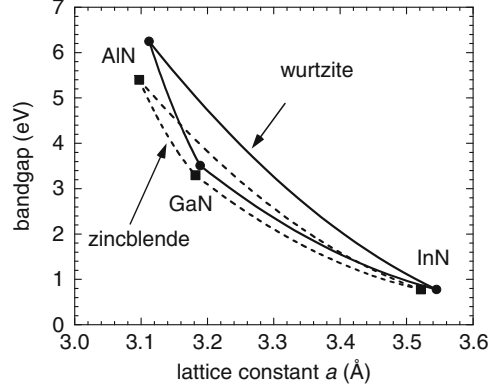


Fig. 1.1. Relation between bandgap energy and lattice constant a for wurtzite or $a_{ZB}/\sqrt{2}$ for zincblende AlN, GaN, InN, and their alloys [1]

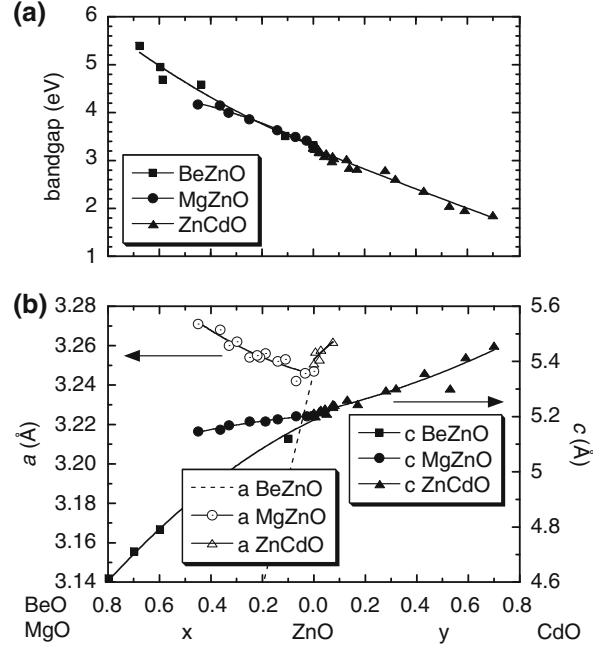


Fig. 1.2. Bandgap energy (a) and lattice constants a and c (b) of wurtzite $\text{Be}_x\text{Zn}_{1-x}\text{O}$ [2], $\text{Mg}_x\text{Zn}_{1-x}\text{O}$ [3, 4], and $\text{Zn}_{1-y}\text{Cd}_y\text{O}$ [4–6] alloy films. Dashed line is a line between a of bulk BeO [7] and a of the ZnO film. Solid lines are quadratic fittings of measured points (symbols)

Figs. 1.3a,b, the WZ structure has AaBbAaBbAaBb... stacking sequence along the [0001] axis, while the ZB structure has AaBbCcAaBbCc... stacking sequence along the [111] axis, where A (a), B (b), and C (c) denote three kinds

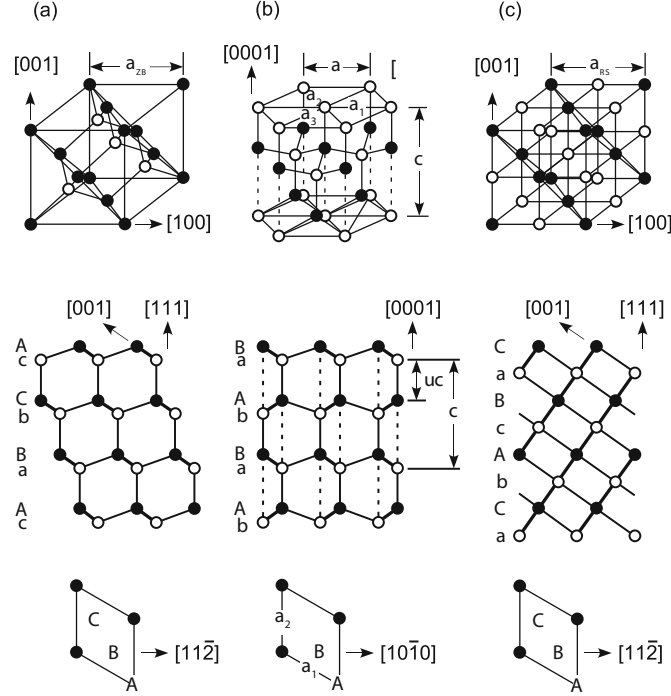


Fig. 1.3. Atomic structure of zincblende (a) wurtzite (b) and rocksalt (c) structures. *Closed circle*, *open circle*, and *thick solid line* represent cation, anion, and projection of two bonds, respectively

of cation (anion) position in the triangular lattice on the (0001) and (111) planes. If the difference between the WZ and ZB structures is only the stacking sequence, WZ lattice constants a and c have relation as $c/a = \sqrt{8/3} = 1.633$ and internal parameter $u = 3/8 = 0.375$, where uc corresponds to the length of the bonds parallel to [0001].

In the WZ structure, however, there are pairs of cation and anion atoms connected by dashed lines along the [0001] direction in Fig. 1.3b and attracted to each other by electrostatic force. It is considered that these electrostatic interactions make WZ–ZnO, AlN, GaN, and InN stabler than ZB–ZnO, AlN, GaN, and InN because ionicity of these compounds is large among the III–V and II–VI compound semiconductors. In the WZ structure, therefore, the length of the dashed lines in Fig. 1.3b tends to be shorter than the ideal one. In fact, c/a is smaller than ideal 1.633 in most of the WZ type materials as shown in Table 1.1. Furthermore, it is easier to shorten the interlayer distances between A–b and B–a than to shorten those between A–a and B–b because the former can be done mostly with angle deformation of the bond pairs. As a result, u is usually larger than ideal 0.375. These structural deformations

Table 1.1. Lattice constants a , c (Å) and internal parameter u of wurtzite structure, lattice constant a_{ZB} (Å) of zincblende structure, and lattice constant a_{RS} (Å) of rocksalt structure. Al_2O_3 is corundum type

	a	c	u	c/a	a_{ZB}	a_{RS}
BeO	2.698 [7]	4.377 [7]	0.378 [7]	1.622	3.81 [8]	3.648 [8]
MgO	3.43 [9]	4.11 [9]	0.5 [9]	1.198		4.216 [10]
ZnO	3.250 [11]	5.204 [11]	0.382 [11]	1.601	4.60 [12]	4.271 [11]
CdO	3.66 [13]	5.86 [13]	0.35 [13]	1.601		4.77 [13]
AlN	3.112 [1]	4.982 [1]	0.380 [14]	1.601	4.38 [1]	
GaN	3.189 [1]	5.185 [1]	0.376 [14]	1.626	4.50 [1]	
InN	3.545 [1]	5.703 [1]	0.377 [14]	1.609	4.98 [1]	
Al_2O_3	4.758 [10]	12.99 [10]				

induce spontaneous polarization; relative displacement of cation to $[000\bar{1}]$ and anion to $[0001]$ from the ideal structure.

Alloys of ZnO with BeO, MgO, and CdO are used to control bandgap of the ZnO system as shown in Fig. 1.2. MgO and CdO are ionic crystals with sixfold coordinated cubic rocksalt (RS) type structure, whose triangular lattice structure in the (111) plane is similar to the hexagonal (0001) plane as shown in Fig. 1.3c. Therefore, WZ $\text{Mg}_x\text{Zn}_{1-x}\text{O}$ [3, 4] and $\text{Zn}_{1-x}\text{Cd}_x\text{O}$ [4–6] have not been obtained when x approaches unity. It was reported that WZ MgO whose u is fixed at $3/8$ is unstable and deforms to be quasi-stable at $u = 0.5$, where a of MgO is larger than that of ZnO as shown in Table 1.1 [9]. The increase of a and decrease of c/a with Mg content x of $\text{Mg}_x\text{Zn}_{1-x}\text{O}$ shown in Fig. 1.2b is consistent with this prediction. It is considered that u increases with x in the case of $\text{Mg}_x\text{Zn}_{1-x}\text{O}$. If $u = 0.5$, MgO deforms to be a fivefold coordinated hexagonal structure, where the bonds shown by the dashed lines in Fig. 1.3b have nearly the same length with other bonds [9]. Bond length and volume per atom of the materials and structures in Table 1.1 are summarized in Table 1.2.

Thermal expansion coefficient of related materials is shown in Table 1.3. Temperature-dependent thermal-expansion coefficients of BeO, ZnO, AlN, GaN, and Al_2O_3 are reported in [15, 16].

1.2.2 Hexagonal Lattice Vectors and Planes

Though three-dimensional space can be indexed by three indices, lattice points of hexagonal lattice are indexed with four indices as $u\ v\ s\ w$, where $u+v+s=0$, to recognize the equivalent directions at a glance. Using three basic lattice vectors \mathbf{a}_1 , \mathbf{a}_2 , \mathbf{a}_3 on the (0001) plane shown in Fig. 1.4a and basic lattice vector \mathbf{c} perpendicular to them, lattice point indexed by $u\ v\ s\ w$ is located at $u\ \mathbf{a}_1 + v\ \mathbf{a}_2 + s\ \mathbf{a}_3 + w\ \mathbf{c} = (2u+v)\ \mathbf{a}_1 + (2v+u)\ \mathbf{a}_2 + w\ \mathbf{c}$ since $\mathbf{a}_3 = -\mathbf{a}_1 - \mathbf{a}_2$ and $s = -u-v$. For example, lattice point \mathbf{a}_1 is represented by $2/3-1/3-1/3\ 0$. Two lattice vectors indexed by $u\ v\ s\ w$ and $u'\ v'\ s'\ 0$ are orthogonal when $u\ u' + v\ v' + s\ s' = 0$.

Table 1.2. Length of the bond parallel to the c -axis b_c (Å), other bond length b_a (Å) and volume per atom v (Å³) of wurtzite structure, bond length b_{ZB} (Å) and volume per atom v_{ZB} (Å³) of zincblende structure, bond length b_{RS} (Å) and volume per atom v_{RS} (Å³) of rocksalt structure evaluated from the parameters in Table 1.1

	b_a	b_c	v	b_{ZB}	v_{ZB}	b_{RS}	v_{RS}
BeO	1.647	1.655	6.90	1.650	6.91	1.824	6.07
MgO	1.980	2.055	10.47			2.108	9.37
ZnO	1.974	1.988	11.90	1.992	12.17	2.136	9.74
CdO	2.289	2.051	17.00			2.385	13.57
AlN	1.894	1.893	10.45	1.897	10.50		
GaN	1.950	1.950	11.42	1.949	11.39		
InN	2.164	2.150	15.52	2.156	15.44		

Table 1.3. Thermal expansion coefficients normal to the c -axis α^\perp (10⁻⁶K⁻¹) and parallel to the c -axis α^\parallel (10⁻⁶K⁻¹) at temperature T (K) of wurtzite type materials except rocksalt type MgO and corundum type Al₂O₃

	T	α^\perp	α^\parallel
BeO [15]	300	5.99	5.35
BeO [15]	700	8.62	7.79
MgO [10]		10.5	
ZnO [15]	300	4.31	2.49
ZnO [15]	700	7.47	4.26
AlN [15]	300	4.35	3.48
AlN [15]	700	4.95	4.22
GaN [15]	300	3.43	3.34
GaN [15]	700	4.91	4.05
InN [10]		4	3
Al ₂ O ₃ [16]	294	4.3	3.9
Al ₂ O ₃ [16]	703	9.2	9.3

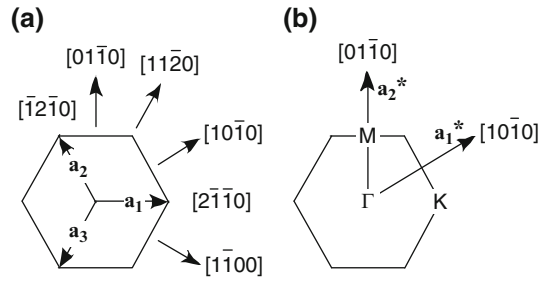


Fig. 1.4. Fundamental lattice vector (a) and reciprocal lattice vector (b) of hexagonal (0001) plane

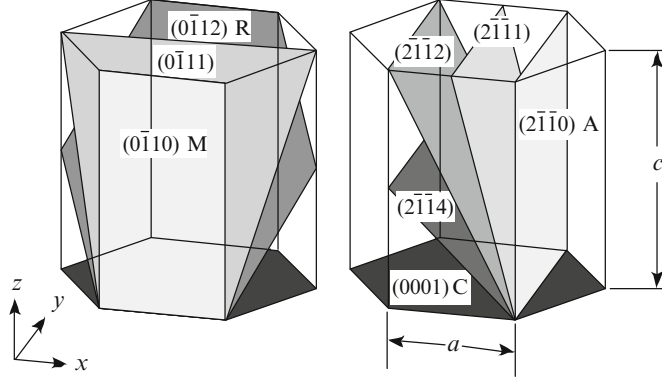


Fig. 1.5. Indices of typical planes in hexagonal structure

Reciprocal lattice vectors \mathbf{a}_1^* , \mathbf{a}_2^* and \mathbf{c}^* have the following relations with the real space vectors \mathbf{a}_1 , \mathbf{a}_2 and \mathbf{c} : $\mathbf{a}_1 \cdot \mathbf{a}_1^* = \mathbf{a}_2 \cdot \mathbf{a}_2^* = \mathbf{c} \cdot \mathbf{c}^* = 2\pi$; \mathbf{a}_1^* , \mathbf{a}_2^* , \mathbf{c}^* are, respectively, perpendicular to \mathbf{a}_2 and \mathbf{c} , \mathbf{a}_1 and \mathbf{c} , and \mathbf{a}_1 and \mathbf{a}_2 . Therefore, the length of \mathbf{a}_1^* , \mathbf{a}_2^* and \mathbf{c}^* are $4\pi/(\sqrt{3}a)$, $4\pi/(\sqrt{3}a)$, and $2\pi/c$, respectively. Reciprocal lattice point

$$\mathbf{g}_{hkl} = h\mathbf{a}_1^* + k\mathbf{a}_2^* + l\mathbf{c}^* \quad (1.1)$$

is indexed by $h\ k\ i\ l$, where $i = -h - k$. When the indices are defined like this, identical directions on the (0001) plane in the real and reciprocal spaces have the same indices as shown in Fig. 1.4. Real-space plane normal to the reciprocal vector \mathbf{g}_{hkl} is also indexed by $h\ k\ i\ l$. Some real space planes are shown in Fig. 1.5. Generally, the $(h\ k\ i\ l)$ plane is not normal to the $[h\ k\ i\ l]$ direction in real space unless $l = 0$ or $h = k = 0$.

1.3 Elastic Strain

1.3.1 Elastic Constants and Elastic Energy Density

Nonzero and independent elastic stiffness constants of hexagonal crystals are c_{11} , c_{12} , c_{13} , c_{33} , and c_{44} and $c_{66} = (c_{11} - c_{12})/2$. The stress components $\tau_{\alpha\beta}$ are linear function of strain components $\varepsilon_{\alpha\beta}$,

$$\begin{bmatrix} \tau_{xx} \\ \tau_{yy} \\ \tau_{zz} \\ \tau_{yz} \\ \tau_{zx} \\ \tau_{xy} \end{bmatrix} = \begin{bmatrix} c_{11} & c_{12} & c_{13} & 0 & 0 & 0 \\ c_{12} & c_{11} & c_{13} & 0 & 0 & 0 \\ c_{13} & c_{13} & c_{33} & 0 & 0 & 0 \\ 0 & 0 & 0 & c_{44} & 0 & 0 \\ 0 & 0 & 0 & 0 & c_{44} & 0 \\ 0 & 0 & 0 & 0 & 0 & c_{66} \end{bmatrix} \begin{bmatrix} \varepsilon_{xx} \\ \varepsilon_{yy} \\ \varepsilon_{zz} \\ \varepsilon_{yz} \\ \varepsilon_{zx} \\ \varepsilon_{xy} \end{bmatrix}, \quad (1.2)$$

Table 1.4. Elastic stiffness coefficients (GPa) of the related materials

	Structure	c_{11}	c_{12}	c_{13}	c_{33}	c_{44}
BeO [17]	WZ	454	85	77	488	155
ZnO [18]	WZ	209.7	121.1	105.1	210.9	42.5
AlN [19]	WZ	396	137	108	373	116
GaN [20]	WZ	390	145	106	398	105
InN [19]	WZ	223	115	92	224	48
MgO [21]	RS	286	87			148
ZnO [12]	ZB	193	139			96
AlN [19]	ZB	304	160			193
GaN [19]	ZB	293	159			155
InN [19]	ZB	187	125			86

where x, y , and z denotes orthogonal $[2\bar{1}\bar{1}0]$, $[01\bar{1}0]$, and $[0001]$ directions and subscripts 1, 2, 3, 4, 5, and 6 denotes xx , yy , zz , yz , zx , and xy , respectively. Elastic energy per unit volume is

$$F = \frac{c_{11}}{2}(\varepsilon_{xx}^2 + \varepsilon_{yy}^2) + \frac{c_{33}}{2}\varepsilon_{zz}^2 + c_{12}\varepsilon_{xx}\varepsilon_{yy} + c_{13}(\varepsilon_{xx} + \varepsilon_{yy})\varepsilon_{zz} + 2c_{44}(\varepsilon_{yz}^2 + \varepsilon_{zx}^2) + 2c_{66}\varepsilon_{xy}^2. \quad (1.3)$$

The elastic stiffness constants of related materials are shown in Table 1.4.

When hydrostatic pressure $\tau_{xx} = \tau_{yy} = \tau_{zz}$ is applied,

$$\begin{aligned} \varepsilon_{xx} &= \varepsilon_{yy}, \\ \varepsilon_{zz} &= \frac{c_{11} + c_{12} - 2c_{13}}{c_{33} - c_{13}}\varepsilon_{xx} \end{aligned} \quad (1.4)$$

is obtained from (1.2). Shear strains are zero under zero shear stress. When stress is applied in one or two directions, stress in the free direction is zero. For example, a normal strain of hexagonal (0001) film under isotropic in-plane stress obeys relation of

$$\begin{aligned} \varepsilon_{xx} &= \varepsilon_{yy}, \\ \varepsilon_{zz} &= -\frac{2c_{13}}{c_{33}}\varepsilon_{xx} \end{aligned} \quad (1.5)$$

because $\tau_{zz} = 0$ and $\tau_{xx} = \tau_{yy}$.

In the WZ structure, spontaneous polarization parallel to c -axis P_{SP} is induced as mentioned in Sect. 1.2.1. External stress also modifies c/a and/or u and induces piezo polarization. Nonzero and independent components of piezoelectric coefficients of the WZ-type materials are e_{31} , e_{33} , and e_{15} . The x , y , and z components of the piezo polarization is

$$\begin{aligned} P_x &= e_{15}\varepsilon_{zx}, \\ P_y &= e_{15}\varepsilon_{yz}, \\ P_z &= e_{31}(\varepsilon_{xx} + \varepsilon_{yy}) + e_{33}\varepsilon_{zz}. \end{aligned} \quad (1.6)$$

Table 1.5. Spontaneous polarization $P_{\text{SP}}(\text{C/m}^2)$ and piezoelectric modulus $e_{ij}(\text{C/m}^2)$ of wurtzite type materials

	P_{SP}	e_{33}	e_{31}	e_{15}
BeO	-0.045 [14]	0.02 [14]	-0.02 [14]	
ZnO	-0.057 [14]	0.89 [14]	-0.51 [14]	-0.45 [22]
AlN	-0.081 [14]	1.46 [14]	-0.60 [14]	-0.48 [23]
GaN	-0.029 [14]	0.73 [14]	-0.49 [14]	-0.3 [24]
InN	-0.032 [14]	0.97 [14]	-0.57 [14]	

P_x and P_y are induced by shear strains, which break the symmetry of the WZ structure. When strain $\varepsilon_{\alpha\beta}$ in (1.6) are replaced with stress $\tau_{\alpha\beta}$, e_{ij} are replaced with d_{ij} that have the following relations to e_{ij} as

$$\begin{aligned}
e_{31} &= d_{31}(c_{11} + c_{12}) + d_{33}c_{13}, \\
e_{33} &= 2d_{31}c_{13} + d_{33}c_{33}, \\
e_{15} &= d_{15}c_{44}.
\end{aligned} \tag{1.7}$$

P_{SP} and e_{ij} of related materials are shown in Table 1.5.

In the case of the cubic crystal, a number of independent elastic stiffness constants are reduced to three as $c_{33} = c_{11}$, $c_{13} = c_{12}$, and $c_{66} = c_{44}$ in (1.2) and (1.3) because the uniaxial anisotropy about c -axis of the hexagonal crystal vanishes. In this case x , y and z denote orthogonal $[100]$, $[010]$ and $[001]$ directions, respectively. The elastic stiffness constants of ZB polymorphs are also shown in Table 1.4. There is only one nonzero and independent component of piezoelectric coefficients for the ZB-type materials. Piezo polarization of the ZB-type materials is

$$\begin{aligned}
P_x &= e_{14}\varepsilon_{yz}, \\
P_y &= e_{14}\varepsilon_{zx}, \\
P_z &= e_{14}\varepsilon_{xy},
\end{aligned} \tag{1.8}$$

where

$$e_{14} = d_{14}c_{44}. \tag{1.9}$$

1.3.2 Strain in Hexagonal- and Cubic-Structure Films

When a hexagonal crystalline film grows in $(01\bar{1}n)$ plane, the surface is normal to $\mathbf{p}_\zeta = \mathbf{g}_{01n}/(2\pi) = (\mathbf{a}_2^* + n\mathbf{c}^*)/(2\pi)$. Using the rectangle coordinate in which x , y , and z are parallel to $[2\bar{1}\bar{1}0]$, $[01\bar{1}0]$ and $[0001]$, $\mathbf{p}_\zeta = (0, 1/b, n/c)$ where $b = \sqrt{3} a/2$. Furthermore $\mathbf{p}_\xi = (1, 0, 0)$ and $\mathbf{p}_\eta = (0, n/c, -1/b)$ can be selected as two orthogonal vectors on the $(01\bar{1}n)$ plane. Then fundamental unit vectors $\mathbf{e}_x = (1, 0, 0)$, $\mathbf{e}_y = (0, 1, 0)$, and $\mathbf{e}_z = (0, 0, 1)$ are expressed as

$$\begin{aligned}
\mathbf{e}_x &= \mathbf{p}_\xi, \\
\mathbf{e}_y &= \frac{bc}{n^2b^2 + c^2}(nb\mathbf{p}_\eta + c\mathbf{p}_\zeta), \\
\mathbf{e}_z &= \frac{bc}{n^2b^2 + c^2}(-c\mathbf{p}_\eta + nb\mathbf{p}_\zeta).
\end{aligned} \tag{1.10}$$

When the in-plane strain along \mathbf{p}_ξ and \mathbf{p}_η are, respectively, ε_ξ and ε_η and surface-normal strain parallel to \mathbf{p}_ζ is ε_ζ , \mathbf{p}_ξ , \mathbf{p}_η , and \mathbf{p}_ζ are deformed to $(1 + \varepsilon_\xi)\mathbf{p}_\xi$, $(1 + \varepsilon_\eta)\mathbf{p}_\eta$, and $(1 + \varepsilon_\zeta)\mathbf{p}_\zeta$. How \mathbf{e}_x , \mathbf{e}_y , and \mathbf{e}_z are deformed with these strains is known by replacing \mathbf{p}_α with $(1 + \varepsilon_\alpha)\mathbf{p}_\alpha$ in (1.10) where $\alpha = \xi, \eta$, and ζ . In this way, strains in the xyz -rectangle coordinate system are represented with strains ε_ξ , ε_η , and ε_ζ as

$$\begin{aligned}
\varepsilon_{xx} &= \varepsilon_\xi, \\
\varepsilon_{yy} &= \frac{n^2b^2\varepsilon_\eta + c^2\varepsilon_\zeta}{n^2b^2 + c^2}, \\
\varepsilon_{zz} &= \frac{c^2\varepsilon_\eta + n^2b^2\varepsilon_\zeta}{n^2b^2 + c^2}, \\
\varepsilon_{yz} &= \frac{nbc(\varepsilon_\zeta - \varepsilon_\eta)}{n^2b^2 + c^2}, \\
\varepsilon_{zx} &= 0, \\
\varepsilon_{xy} &= 0,
\end{aligned} \tag{1.11}$$

and strain energy density of (1.3) is represented with ε_ξ , ε_η , and ε_ζ . Surface-normal strain ε_ζ that minimizes F is given by solving $\partial F / \partial \varepsilon_\zeta = 0$ as

$$\varepsilon_\zeta = - \frac{(n^2b^2 + c^2)(n^2b^2c_{13} + c^2c_{12})\varepsilon_\xi + \{n^2b^2c^2(c_{11} + c_{33} - 4c_{44}) + (n^4b^4 + c^4)c_{13}\}\varepsilon_\eta}{c^4c_{11} + n^4b^4c_{33} + 2n^2b^2c^2(c_{13} + 2c_{44})}, \tag{1.12}$$

where $b = \sqrt{3}a/2$.

When a hexagonal crystalline film grows in $(2\bar{1}\bar{1}n)$ plane, the surface is normal to $\mathbf{p}_\zeta = (2\mathbf{a}_1^* - \mathbf{a}_2^* + n\mathbf{c}^*)/(2\pi) = (1/b, 0, n/c)$, where $b = a/2$. In this case, $\mathbf{p}_\xi = (n/c, 0, -1/b)$ and $\mathbf{p}_\eta = (0, 1, 0)$ can be selected as two orthogonal vectors on the $(2\bar{1}\bar{1}n)$ plane. Therefore, surface-normal strain ε_ζ is also given by (1.12), where $b = a/2$, ε_ξ and ε_η are in-plane strain along \mathbf{p}_η and \mathbf{p}_ξ , respectively because x and y , \mathbf{p}_ξ and \mathbf{p}_η are respectively exchanged with each other in comparison with the case of the $(01\bar{1}n)$ plane.

When a cubic crystalline film grows in $(mn1)$ plane, surface is normal to $\mathbf{p}_\zeta = (m, n, 1)$, where $\mathbf{p}_\xi = (n^2 + 1, -mn, -m)$ and $\mathbf{p}_\eta = (0, 1, -n)$ can be selected as two orthogonal vectors on the $(mn1)$ plane. In this case x , y , and z components are parallel to $[100]$, $[010]$, and $[001]$ directions, respectively. Surface-normal strain ε_ζ is given by solving $\partial F / \partial \varepsilon_\zeta = 0$ as

$$\varepsilon_\zeta = -2\varepsilon_{||} \frac{(m^4 + n^4 + 1)c_{12} + 2(m^2n^2 + m^2 + n^2)(c_{11} + c_{12} - 2c_{44})}{(m^4 + n^4 + 1)c_{11} + 2(m^2n^2 + m^2 + n^2)(c_{12} + 2c_{44})}, \quad (1.13)$$

where $\varepsilon_{||}$ is in-plane strain, which is assumed to be isotropic.

1.4 Electronic Structure

1.4.1 Bandgap and Band-Edge Electronic Structure

The first Brillouin zone of a hexagonal crystal is a hexagonal prism of height $2\pi/c$. The boundary of the zone at $k_z = 0$ (k_z is a component of the wave vector \mathbf{k} parallel to c -axis) is shown in Fig. 1.4b, where symbols for symmetric points are also shown. The point at $k_z = \pi/c$ just above the Γ , K, and M points are denoted as A, H, and L, respectively.

BeO, ZnO, AlN, GaN, and InN are direct-bandgap semiconductors, whose band edge is located at the Γ point. Temperature dependence of the bandgap energy E_g can be expressed by the Varshni formula

$$E_g(T) = E_g(0) - \frac{\alpha T^2}{T + \beta}. \quad (1.14)$$

Bandgap energy, Varshni parameters α and β are listed in Table 1.6. Bandgap energy of alloy $A_{1-x}B_xC$ is approximately represented by a quadratic function of x as

$$E_g(x) = (1 - x)E_g^{\text{AC}} + xE_g^{\text{BC}} - bx(1 - x), \quad (1.15)$$

where b is bowing parameter. Figure 1.1 is drawn using bandgap energies and bowing parameters of III-nitrides shown in Tables 1.6 and 1.7.

Energy dispersion around the bottom of conduction band (mainly consists of anti-bonding state of cation s electrons) can be represented as

$$E_c(\mathbf{k}) = E_{c0} + \frac{\hbar^2}{2m_0m_e^\perp}(k_x^2 + k_y^2) + \frac{\hbar^2}{2m_0m_e^\parallel}k_z^2 + a_2(\varepsilon_{xx} + \varepsilon_{yy}) + a_1\varepsilon_{zz}, \quad (1.16)$$

Table 1.6. Bandgap energy E_g (eV) at temperature T (K) and Varshni parameters α (meV/K) and β (K)

	Structure	T	E_g	α	β
BeO	WZ	77	10.63 [25]		
ZnO	WZ	4.2	3.437 [26]		
AlN	WZ	0	6.25 [1]	1.799 [1]	1462 [1]
GaN	WZ	0	3.510 [1]	0.909 [1]	830 [1]
InN	WZ	0	0.78 [1]	0.245 [1]	624 [1]
AlN	ZB	0	5.4 [1]	0.593 [1]	600 [1]
GaN	ZB	0	3.299 [1]	0.593 [1]	600 [1]
InN	ZB	0	0.78 [1]	0.245 [1]	624 [1]

Table 1.7. Bowing parameter (eV) recommended for both wurtzite and zincblende type III-nitrides [1]

	b
AlGaIn	0.7
GaInN	1.4
AlInN	2.5

Table 1.8. Electron and hole effective mass (in the unit of m_0) of wurtzite type materials

	m_e^{\parallel}	m_e^{\perp}	m_A^{\parallel}	m_B^{\parallel}	m_C^{\parallel}	m_A^{\perp}	m_B^{\perp}	m_C^{\perp}
BeO [27]	0.58	0.74	12.01			2.44		
ZnO [28]	0.23	0.21	2.74	3.03	0.27	0.54	0.55	1.12
AlN [29]	0.33	0.25	0.25	3.68	3.68	3.68	6.33	0.25
GaN [29]	0.20	0.18	1.10	1.10	0.15	1.65	0.15	1.10
InN [30]	0.11	0.10	1.67	1.67	0.10	1.61	0.11	1.67

Table 1.9. Deformation potential (eV) of wurtzite type materials

	a_1	a_2	D_1	D_2	D_3	D_4	D_5	D_6
ZnO [31]			3.9	4.13	1.15	-1.22	-1.53	-2.88
AlN [1]	-3.4	-11.8	-17.1	7.9	8.8	-3.9	-3.4	-3.4
GaN [1]	-4.9	-11.3	-3.7	4.5	8.2	-4.1	-4.0	-5.5
InN [1]	-3.5	-3.5	-3.7	4.5	8.2	-4.1	-4.0	-5.5

where E_{c0} is band edge energy of the conduction band, \hbar is Planck constant divided by 2π , m_0 is rest mass of electron in vacuum, m_e^{\perp} and m_e^{\parallel} are effective mass of the conduction electron, a_1 and a_2 are deformation potential of the conduction band, k_x , k_y , and k_z are x , y , and z component of wave vector \mathbf{k} , superscript \parallel and \perp denotes parallel and perpendicular to c -axis, respectively. The effective mass and the deformation potential are shown in Tables 1.8 and 1.9.

Figure 1.6 illustrates energy-level splittings for WZ and ZB semiconductors at the top of the valence band, which mainly consists of anion p electrons. The spin-orbit coupling proportional to $l \cdot s = (j^2 - l^2 - s^2)/2$ splits the energy level according to j , which is angular momentum composed of orbital (l) and spin (s) angular momentums. In WZ structure, crystal-field splitting appears owing to the structural anisotropy between parallel to and normal to the c -axis. The l_z and j_z in Fig. 1.6 are c -axis component of l and j , respectively. The crystal-field splitting Δ_{cr} and the spin-orbit splitting Δ_{so} are shown in Table 1.10. As for AlN, the crystal-field split-off band, which is lowest in Fig. 6, moves to the top because Δ_{cr} of AlN is negative.

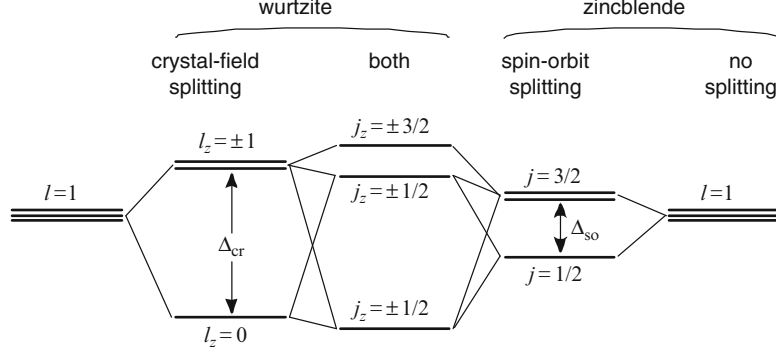


Fig. 1.6. Schematic energy diagram of valence-band top for wurtzite and zincblende semiconductors

Table 1.10. Crystal-field splitting Δ_{cr} and spin-orbit splitting Δ_{so} (meV) of wurtzite type materials

	Δ_{cr}	Δ_{so}
ZnO [32]	43	16
AlN [29]	-58.5	20.4
GaN [29]	72.9	15.5
InN [1]	40	5

1.4.2 Bir-Pikus Hamiltonian

Energy dispersion around valence band maximum at Γ point can be obtained by calculating eigen values of the following Bir-Pikus Hamiltonian matrix $H_{BP}(\mathbf{k})$ for WZ semiconductors as a function of \mathbf{k} [29, 33].

$$\mathbf{H}_{BP}(\mathbf{k}) = \begin{bmatrix} F & 0 & -H^* & 0 & K^* & 0 \\ 0 & G & \Delta & -H^* & 0 & K^* \\ -H & \Delta & \lambda & 0 & I^* & 0 \\ 0 & -H & 0 & \lambda & \Delta & I^* \\ K & 0 & I & \Delta & G & 0 \\ 0 & K & 0 & I & 0 & F \end{bmatrix}, \quad (1.17)$$

Where

$$F = \Delta_1 + \Delta_2 + \lambda + \theta, \quad (1.18)$$

$$G = \Delta_1 - \Delta_2 + \lambda + \theta, \quad (1.19)$$

$$\lambda = A_1 k_z^2 + A_2 (k_x^2 + k_y^2) + \lambda_\epsilon, \quad (1.20)$$

$$\lambda_\epsilon = D_1 \epsilon_{zz} + D_2 (\epsilon_{xx} + \epsilon_{yy}), \quad (1.21)$$

$$\theta = A_3 k_z^2 + A_4 (k_x^2 + k_y^2) + \theta_\epsilon, \quad (1.22)$$

Table 1.11. Valence band effective-mass parameters (in the unit of $\hbar^2/(2m_0) = 3.81 \text{ eV}\text{\AA}^2$) of wurtzite type materials

	A_1	A_2	A_3	A_4	A_5	A_6
ZnO [28]	-3.78	-0.44	3.45	-1.63	1.68	-2.23
AlN [29]	-3.95	-0.27	3.68	-1.84	-1.95	-2.91
GaN [29]	-6.56	-0.91	5.65	-2.83	-3.13	-4.86
InN [30]	-9.28	-0.60	8.68	-4.34	-4.32	-6.08

$$\theta_\varepsilon = D_3\varepsilon_{zz} + D_4(\varepsilon_{xx} + \varepsilon_{yy}), \quad (1.23)$$

$$\Delta = \sqrt{2}\Delta_3, \quad (1.24)$$

$$H = (iA_6k_z - A_7)(k_x + ik_y) + iD_6(\varepsilon_{zx} + i\varepsilon_{yz}), \quad (1.25)$$

$$I = (iA_6k_z + A_7)(k_x + ik_y) + iD_6(\varepsilon_{zx} + i\varepsilon_{yz}), \quad (1.26)$$

$$K = A_5(k_x + ik_y)^2 + D_5(\varepsilon_{xx} - \varepsilon_{yy} + 2i\varepsilon_{xy}), \quad (1.27)$$

$\Delta_1 = \Delta_{\text{cr}}, \Delta_2 = \Delta_3 = \Delta_{\text{so}}/3, A_i$ are Luttinger-like parameters related to effective mass of holes, D_i are deformation potentials, and superscript * denotes complex conjugate. The strain dependent terms are given by replacing A_i and $k_\alpha k_\beta$ with D_i and $\varepsilon_{\alpha\beta}$, where $\alpha, \beta = x, y, z$. λ_ε is common to all the diagonal elements and corresponds to the shift of the whole valence band, relative to the conduction band minimum under strain. θ_ε corresponds to variation in Δ_1 under strain. The parameters for the related WZ semiconductors are shown in Tables 1.9, 1.10, and 1.11. Sign of D_i is opposite to that of [31] because D_i in [31] is defined as a deformation potential for the bandgap. The six basis functions are as follows:

$$u_1 = \sqrt{\frac{1}{2}}|(X + iY), \uparrow\rangle, u_2 = \sqrt{\frac{1}{2}}|(X + iY), \downarrow\rangle, \quad (1.28)$$

$$u_3 = |Z, \uparrow\rangle, u_4 = |Z, \downarrow\rangle, \quad (1.29)$$

$$u_5 = \sqrt{\frac{1}{2}}|(X - iY), \uparrow\rangle, u_6 = \sqrt{\frac{1}{2}}|(X - iY), \downarrow\rangle, \quad (1.30)$$

where $|\uparrow\rangle$ and $|\downarrow\rangle$ are up and down spin functions, respectively, l_z of u_1 and u_2 is 1, u_3 and u_4 is 0, and u_5 and u_6 is -1 . Energy and wave function at any \mathbf{k} and strain can be numerically calculated. Fortunately, in some limited cases, $H_{\text{BP}}(\mathbf{k})$ can be diagonalized analytically.

First, if $k_x = k_y = 0$, $\varepsilon_{xx} = \varepsilon_{yy}$, and shear strains are zero, then H , I , and K become zero. Symmetry of the WZ structure is kept under this kind of strain, which replaces Δ_1 with $\Delta_1 + \theta_\varepsilon$. Then $H_{\text{BP}}(\mathbf{k})$ consists of 1^2 , 2^2 , 2^2 , and 1^2 block matrices, whose basis functions are u_1 , u_2 and u_3 , u_4 and u_5 , and u_6 . Eigen energies are

$$E_1^{\parallel} = F = \Delta_1 + \theta_\varepsilon + \Delta_2 + (A_1 + A_3)k_z^2 + \lambda_\varepsilon, \quad (1.31)$$

$$\begin{aligned} E_{\pm}^{\parallel} &= \frac{G + \lambda \pm \sqrt{(G - \lambda)^2 + 4\Delta^2}}{2} \\ &= \frac{\Delta_1 + \theta_\varepsilon - \Delta_2 + (2A_1 + A_3)k_z^2 \pm \sqrt{(\Delta_1 + \theta_\varepsilon - \Delta_2 + A_3k_z^2)^2 + 8\Delta_3^2}}{2} + \lambda_\varepsilon. \end{aligned} \quad (1.32)$$

Eigen function of E_1^{\parallel} is u_1 or u_6 ($j_z = 3/2$) having Γ_9 symmetry and those of E_{\pm}^{\parallel} are a mixture of u_2 and u_3 or a mixture of u_4 and u_5 ($j_z = 1/2$) having Γ_7 symmetry. The three bands at the valence-band top of the WZ semiconductors (Fig. 1.6) are called A, B, and C bands from upper band to lower band. Generally $\Delta_{\text{cr}} > \Delta_{\text{so}} > 0$ is satisfied. When $\Delta_{\text{cr}} + \theta_\varepsilon > \Delta_{\text{so}} > 0$, E_1^{\parallel} , E_+^{\parallel} , and E_-^{\parallel} with Γ_9 , Γ_7 (mainly u_2 or u_5), and Γ_7 (mainly u_3 or u_4) symmetry correspond to the A, B, and C bands, respectively. In the case of AlN, Δ_{cr} is negative. When $-(\Delta_{\text{cr}} + \theta_\varepsilon) > \Delta_{\text{so}} > 0$, E_+^{\parallel} , E_1^{\parallel} , and E_-^{\parallel} with Γ_7 (mainly u_3 or u_4), Γ_9 , and Γ_7 (mainly u_2 or u_5) symmetry correspond to the A, B, and C bands, respectively. In the case of ZnO, it had been thought that Δ_2 and Δ_3 are negative. When $\Delta_{\text{cr}} + \theta_\varepsilon > -\Delta_{\text{so}} > 0$, E_+^{\parallel} , E_1^{\parallel} , and E_-^{\parallel} with Γ_7 (mainly u_2 or u_5), Γ_9 , and Γ_7 (mainly u_3 or u_4) symmetry correspond to the A, B, and C bands, respectively. It was supported by recent optical measurements, however, that Δ_2 and Δ_3 of ZnO are positive [32]. Anyway since $|\Delta_{\text{so}}|$ is small, interband optical transitions between the conduction band and the E_+^{\parallel} (E_-^{\parallel} in the case of AlN) band as well as the E_1^{\parallel} band are strong for the light polarized perpendicular to the c -axis and that of the E_-^{\parallel} (E_+^{\parallel} in the case of AlN) band is strong for the light polarized parallel to the c -axis.

Effective mass of the hole in k_z direction is obtained from the coefficient of k_z^2 term as

$$m_1^{\parallel} = -\frac{1}{A_1 + A_3}, \quad (1.33)$$

$$m_+^{\parallel} = -\frac{1}{A_1 + A_3}, \quad (1.34)$$

$$m_-^{\parallel} = -\frac{1}{A_1}, \quad (1.35)$$

for the E_1^{\parallel} , E_+^{\parallel} and E_-^{\parallel} band, respectively, if Δ_3 is disregarded when a comparatively wide range of k_z is considered above room temperature. In the case of AlN, m_+^{\parallel} and m_-^{\parallel} must be replaced with each other.

Next if $k_z = 0$, $A_7 = 0$, and shear strains are zero, then H and I become zero. In order to simplify further, $\Delta_3 = 0$ is assumed since the crystal field Δ_1 mainly characterizes the valence band-edge structures of the WZ crystals. Then, $H_{\text{BP}}(\mathbf{k})$ is decomposed into 2^2 , 2^2 , 1^2 , and 1^2 blocks, whose basic functions are u_1 and u_5 , u_2 and u_6 , u_3 , and u_4 [29]. Eigen energies are

$$E_{\pm}^{\perp} = \frac{F + G \pm \sqrt{(F - G)^2 + 4|K|^2}}{2} = \Delta_1 + \theta_{\varepsilon} + (A_2 + A_4)(k_x^2 + k_y^2) \pm \sqrt{\Delta_2^2 + A_5^2(k_x^2 + k_y^2)^2} + \lambda_{\varepsilon}, \quad (1.36)$$

$$E_3^{\perp} = \lambda = A_2(k_x^2 + k_y^2) + \lambda_{\varepsilon}. \quad (1.37)$$

The effective mass of the hole in k_x and k_y direction is obtained as

$$m_{\pm}^{\perp} = -\frac{1}{A_2 + A_4 \pm |A_5|}, \quad (1.38)$$

$$m_3^{\perp} = -\frac{1}{A_2}, \quad (1.39)$$

for the E_{\pm}^{\perp} and E_3^{\perp} band, respectively. Generally (in the case of AlN), E_{+}^{\perp} , E_{-}^{\perp} , and E_3^{\perp} (E_3^{\perp} , E_{+}^{\perp} , and E_{-}^{\perp}) correspond to the A, B, and C bands, respectively.

1.4.3 Valence Band-Edge and Bandgap of Strained ZnO

Valence band dispersion curves of ZnO at various isotropic in-plane strain $\varepsilon_{xx} = \varepsilon_{yy}$, where ε_{zz} is given by (1.5), are shown in Fig. 1.7 using ZnO parameters in Tables 1.9, 1.10, and 1.11.

Solid lines are calculated numerically, while dashed lines are calculated for $\Delta_3 = 0$ using (1.36) and (1.37) along k_x axis and (1.31) and (1.32) along k_z axis. Here $\Delta_3 = 0$ is assumed even in (1.31) and (1.32) to let the dashed lines be continuous. Of course (1.31) and (1.32) give identical lines with the solid lines without such assumption. Around $\varepsilon_{xx} = 1.2\%$ spin-orbit interaction becomes relatively important and the error due to the omission of Δ_3 is not small near the Γ point because the substantial crystal-field splitting $\Delta_1 + \theta_{\varepsilon}$, which includes the effect of strain, approaches to be zero. Valence band structure of the strain free AlN is similar to that of ZnO at $\varepsilon_{xx} = 2\%$ shown in Fig. 1.7 because $\Delta_1 + \theta_{\varepsilon}$ is negative in this case.

ZnO bandgaps between the bottom of the conduction band and the top of the A, B, and C bands are shown in Fig. 1.8 as a function of isotropic strain in c -plane. Here, fundamental bandgap at zero strain is set to be $E_{g0} = 3.4368$ eV [26]. The solid line shows the case when $\tau_{zz} = 0$, $\tau_{xx} = \tau_{yy}$, and $\varepsilon_{zz} = -0.997 \varepsilon_{xx}$ from (1.5). Fundamental bandgap E_g is expected to vary as $E_g = E_{g0} - 0.787 \varepsilon_{xx}$ eV when (1.31) and the ZnO deformation potentials in Table 1.9 are used. However, the slope is about half compared with the one measured for ZnO (0001) thin films [34]. The deformation potentials in Table 1.9 are measured for bulk ZnO under uniaxial stress [31]. The dashed lines show the case under hydrostatic pressure, where $\varepsilon_{zz} = 1.14 \varepsilon_{xx}$ from

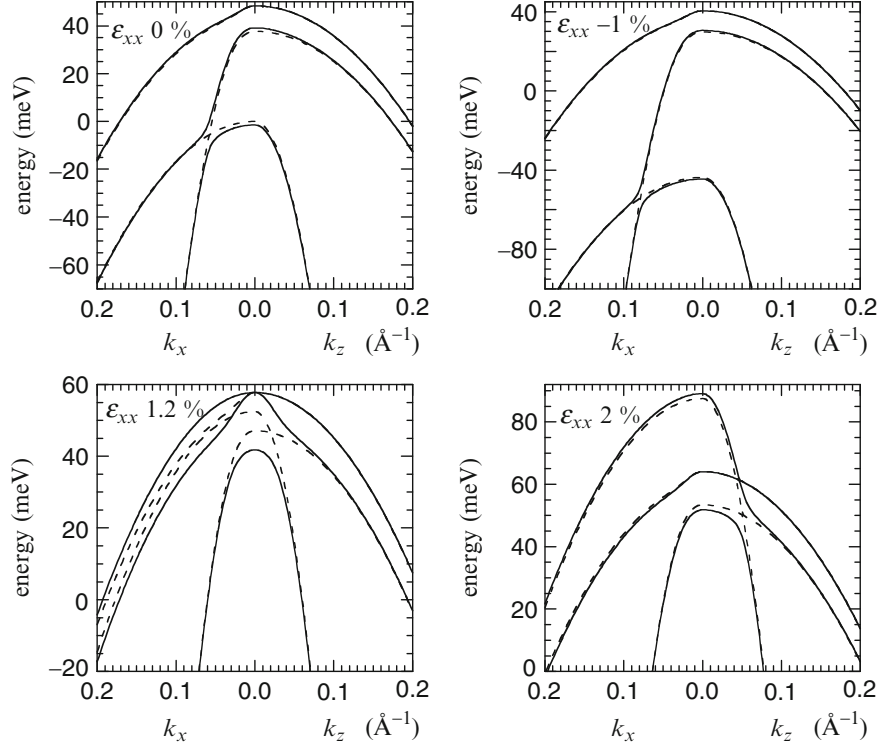


Fig. 1.7. ZnO band structures near the valence-band top at various isotropic in-plane strain $\varepsilon_{xx} = \varepsilon_{yy}$

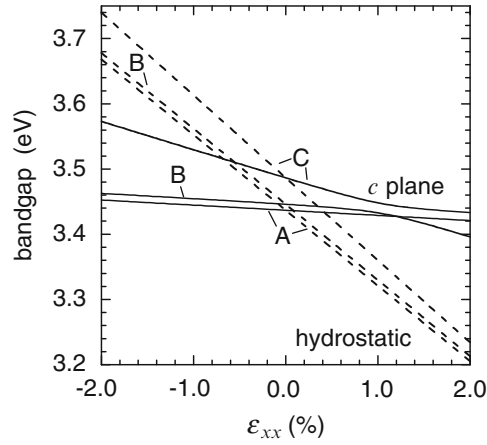


Fig. 1.8. Bandgap energy between conduction band minimum and A, B, and C valence band maximum of ZnO as a function of in-plane strain under hydrostatic (dashed line) and isotropic in-plane (solid line) stress

(1.4). Fundamental bandgap $E_g = E_{g0} - 11.57 \varepsilon_{xx}$ eV decreases with increasing interatomic distance. When this strain coefficient is converted using (1.2) and (1.4), hydrostatic pressure coefficient of $25.69 \text{ meV GPa}^{-1}$, which is in fair agreement with measured values $23.5 \sim 29.7 \text{ meV GPa}^{-1}$ [35], is obtained.

1.4.4 Exciton Binding Energy

When electron-hole pair of exciton is treated like electron and proton of hydrogen atom, binding energy and Bohr radius of 1S exciton are $E_{\text{ex}0} = E_H \mu / \varepsilon(0)^2$, and $a_{\text{ex}0} = a_B \varepsilon(0) / \mu$, respectively, where $E_H = 13.6 \text{ eV}$ and $a_B = 0.529 \text{ \AA}$ are binding energy and Bohr radius of 1s electron of hydrogen atom, respectively. Reduced mass μ and static dielectric constant $\varepsilon(0)$ are given as [36]

$$\frac{1}{\mu} = \frac{1}{m_e} + \frac{1}{m_h}, \quad (1.40)$$

$$\frac{1}{m_e} = \frac{2}{3m_e^\perp} + \frac{\varepsilon^\perp(0)}{3\varepsilon^\parallel(0)m_e^\parallel}, \quad (1.41)$$

$$\frac{1}{m_h} = \frac{2}{3m_h^\perp} + \frac{\varepsilon^\perp(0)}{3\varepsilon^\parallel(0)m_h^\parallel}, \quad (1.42)$$

$$\varepsilon(0) = \sqrt{\varepsilon^\parallel(0)\varepsilon^\perp(0)}. \quad (1.43)$$

The electron and hole effective mass and the dielectric constant of related WZ materials are listed in Tables 1.8 and 1.12. The data in Table 1.12 fulfill the Lyddane–Sachs–Teller relation $\omega_{\text{LO}}^2 / \omega_{\text{TO}}^2 = \varepsilon(0) / \varepsilon(\infty)$ except 15% discrepancy for InN, where $\varepsilon(\infty)$ is the dielectric constant at high frequency, and ω_{LO} and ω_{TO} are longitudinal and transverse optical-phonon frequency, respectively. $E_{\text{ex}0}$ and $a_{\text{ex}0}$ calculated for A exciton, where $m_h = m_A$, using these values are shown in Table 1.13. In the cases of ZnO and AlN, $E_{\text{ex}0}$ estimated with the static Coulomb potential is smaller than the observed exciton binding energy E_{ex} . When electrons and holes move in a polar crystal,

Table 1.12. Dielectric constant and optical phonon energy (meV) of wurtzite type materials except rocksalt type MgO

	$\varepsilon^\parallel(0)$	$\varepsilon^\perp(0)$	$\varepsilon^\parallel(\infty)$	$\varepsilon^\perp(\infty)$	$\hbar \omega_{\text{LO}}$	$\hbar \omega_{\text{TO}}$
BeO	7.65 [37]	6.94 [37]	2.99 [37]	2.95 [37]	135.2 [37]	87.2 [37]
MgO	9.8 [21]		2.95 [21]		92.2 [21]	49.4 [21]
ZnO	8.49 [38]	7.40 [38]	3.72 [38]	3.68 [38]	72.8 [39]	51.0 [39]
AlN	8.5 [10]	8.5 [10]	4.76 [10]	4.76 [10]	112.6 [40]	81.1 [40]
GaN	9.5 [41]	10.4 [41]	5.35 [10]	5.35 [10]	90.6 [40]	68.3 [40]
InN	15 [10]	15 [10]	8.4 [10]	8.4 [10]	86.0 [40]	59.3 [40]

Table 1.13. Exciton binding energy: E_{ex} (experiment); E_{ex0} (hydrogen like); and E_{ex1} (Pollmann–Büttner–Kane) (meV), Bohr radius: a_{ex0} (hydrogen like) and a_{ex1} (Pollmann–Büttner–Kane) (Å), electron–polaron radius r_e (Å), and hole–polaron radius r_h (Å)

	E_{ex}	E_{ex0}	a_{ex0}	r_e	r_h	E_{ex1}	a_{ex1}
BeO	175 [25]	149	6.6	6.3	2.9	389	3.0
ZnO	60 [26]	37.5	24.2	15.2	8.4	61.0	14.5
AlN	57 [42]	36.3	23.4	11.1	7.2	45.1	18.0
GaN	23.44 [43]	22.0	32.9	15.2	5.6	25.3	27.7
InN		5.9	81.8	20.7	5.2	6.1	78.0

they interact with nearby ions and distort the lattice. Therefore, it is better to describe the electron and hole as polaron in II-oxides and III-nitrides. Pollmann and Büttner investigated the interaction of Wannier excitons with LO-phonon field. When the exciton Bohr radius is sufficiently larger than the polaron radii, effective electron-hole interaction potential approximates [44]

$$V_{\text{PB}}(r) = -\frac{e^2}{4\pi\epsilon(0)r} - \frac{e^2}{4\pi\epsilon^*(m_h - m_e)r} \left\{ m_h \exp\left(-\frac{r}{r_h}\right) - m_e \exp\left(-\frac{r}{r_e}\right) \right\}, \quad (1.44)$$

where r is the distance between the electron and hole, $r_h = \hbar/(2m_h\hbar\omega_{\text{LO}})^{1/2}$ is the hole–polaron radius, and $r_e = \hbar/(2m_e\hbar\omega_{\text{LO}})^{1/2}$ is the electron–polaron radius, and $1/\epsilon^* = 1/\epsilon(\infty) - 1/\epsilon(0)$. Equation (1.44) indicates that effective dielectric constant approaches $\epsilon(\infty)$ as the electron–hole distance r decreases to be smaller than the polaron radii. Later, Kane added the correction for the polaron mass and provided tabulated functions to estimate the excitonic–polaron binding energy (E_{ex1}) by variational method [45]. Trial wave function is hydrogen 1s type $\exp(-r/a)/(\pi a^3)^{1/2}$ and minimized $-E_{\text{ex1}}$ is obtained at the variational parameter $a = a_{\text{ex1}}$. The binding energy E_{ex1} and the Bohr radius a_{ex1} corrected by this method with parameters listed in Tables 1.8 and 1.12 are shown in Table 1.13. The correction by the polaron effect is large for II-oxide owing to the small a_{ex1}/r_e and a_{ex1}/r_h ratios.

References

1. I. Vurgaftman, J.R. Meyer, J. Appl. Phys. **94**, 3675 (2003)
2. Y.R. Ryu et al., Appl. Phys. Lett. **88**, 052103 (2006)
3. A. Ohtomo et al., Appl. Phys. Lett. **72**, 2466 (1998)
4. T. Makino et al., Appl. Phys. Lett. **78**, 1237 (2001)
5. A. Nakamura et al., Jpn. J. Appl. Phys. **43**, L1452 (2004)
6. J. Ishihara et al., Appl. Phys. Lett. **89**, 091914 (2006)
7. R.M. Hazen, L.W. Finger, J. Appl. Phys. **59**, 3728 (1986)

8. C.J. Park et al., Phys. Rev. B **59**, 13501 (1999)
9. S. Limpijumnong, W.R.L. Lambrecht, Phys. Rev. B **63**, 104103 (2001)
10. H. Morkoç et al., J. Appl. Phys. **76**, 1363 (1994)
11. H. Karzel et al., Phys. Rev. B **53**, 11425 (1996)
12. Ü. Özgür et al., J. Appl. Phys. **98**, 041301 (2005)
13. R.J. Guerrero-Moreno, N. Takeuchi, Phys. Rev. B **66**, 205205 (2002)
14. F. Bernardini, V. Fiorentini, D. Vanderbilt, Phys. Rev. B **56**, R10024 (1997)
15. H. Iwanaga, A. Kunishige, S. Takeuchi, J. Mater. Sci. **35**, 2451 (2000)
16. M. Leszczynski, J. Appl. Phys. **76**, 4909 (1994)
17. A. Bosak et al., Phys. Rev. B **77**, 224303 (2008)
18. T.B. Bateman, J. Appl. Phys. **33**, 3309 (1962)
19. A.F. Wright, J. Appl. Phys. **82**, 2833 (1997)
20. A. Polian, M. Grimsditch, I. Grzegory, J. Appl. Phys. **79**, 3343 (1996)
21. C. Kittel, *Introduction to Solid State Physics*, 4th edn. (Wiley, New York, 1971)
22. C. Carlotti et al., Appl. Phys. Lett. **51**, 1889 (1987)
23. K. Tsubouchi, N. Mikoshiba, IEEE Trans. Sonics Ultrason. **SU-32**, 634 (1985)
24. G.D. O'Clock, M.T. Duffy, Appl. Phys. Lett. **23**, 55 (1973)
25. D.M. Roessler, W.C. Walker, E. Loh, J. Phys. Chem. Solids **30**, 157 (1969)
26. S.F. Chichibu et al., J. Appl. Phys. **93**, 756 (2003)
27. Y.N. Xu, W.Y. Ching, Phys. Rev. B **48**, 4335 (1993)
28. W.R.L. Lambrecht et al., Phys. Rev. B **65**, 075207 (2002)
29. M. Suzuki, T. Uenoyama, A. Yanase, Phys. Rev. B **52**, 8132 (1995)
30. Y.C. Yeo, T.C. Chong, M.F. Li, J. Appl. Phys. **83**, 1429 (1998)
31. J. Wrzesinski, D. Fröhlich, Phys. Rev. B **56**, 13087 (1997)
32. D.C. Reynolds et al., Phys. Rev. B **60**, 2340 (1999)
33. G.L. Bir, G.E. Pikus, *Symmetry and Strain-Induced Effects in Semiconductors* (Wiley, New York, 1974)
34. Th. Gruber et al., J. Appl. Phys. **96**, 289 (2004)
35. S.J. Chen et al., J. Appl. Phys. **99**, 066102 (2006)
36. A.V. Rodina et al., Phys. Rev. B **64**, 115204 (2001)
37. E. Loh, Phys. Rev. **166**, 673 (1968)
38. H. Yoshikawa, S. Adachi, Jpn. J. Appl. Phys. **36**, 6237 (1997)
39. T.C. Damen, S.P.S. Porto, B. Tell, Phys. Rev. **142**, 570 (1966)
40. K. Kim, W.R.L. Lambrecht, B. Segall, Phys. Rev. B **53**, 16310 (1996); **56**, 7018 (1997)
41. A.S. Barker Jr., M. Ilegems, Phys. Rev. B **7**, 743 (1973)
42. Y. Yamada et al., Appl. Phys. Lett. **92**, 131912 (2008)
43. K. Torii et al., Phys. Rev. B **60**, 4723 (1999)
44. J. Pollmann, H. Büttner, Phys. Rev. B **16**, 4480 (1977)
45. E.O. Kane, Phys. Rev. B **18**, 6849 (1978)



<http://www.springer.com/978-3-540-88846-8>

Oxide and Nitride Semiconductors
Processing, Properties, and Applications
Yao, T.; Hong, S.-K. (Eds.)
2009, XIV, 518 p., Hardcover
ISBN: 978-3-540-88846-8